The physics of nanowire superconducting single-photon detectors

Renema, J.J.

Chapter 3

Universal Response Curve for Nanowire Superconducting Single-Photon Detectors

Using detector tomography, we investigate the detection mechanism in NbN-based superconducting single-photon detectors (SSPDs). We demonstrate that the detection probability uniquely depends on a particular linear combination of bias current and energy, for a large variation of bias currents, input energies and detection probabilities, producing a universal detection curve. We obtain this result by studying multiphoton excitations in a nanodetector with a sparsity-based tomographic method that allows factoring out of the optical absorption. We discuss the implication of our model system for the understanding of meander-type SSPDs[1].

3.1 Introduction

Nanowire Superconducting Single-Photon Detectors (SSPDs) [1] have high detection efficiency [55], low dark counts, low jitter and a broadband absorption spectrum [56]. This makes them suitable for many applications including quantum optics [57, 58, 59, 60], quantum key distribution [5, 61], optical coherence domain reflectometry [62] and interplanetary communication [6]. These detectors typically consist of a thin nanowire ($\sim$4 nm x 100 nm) of superconducting material, such as NbN [1], TaN [20], NbTiN [63], Nb

[1] This chapter is based on J.J. Renema *et al.*, Phys. Rev. B **87** (17), 174526 (2013).

[64], or WSi [55], which is typically fabricated in a meander shape to cover an active area of 25-1600 μm^2 [65]. The absorption of a single photon in the nanowire results in the creation of a a region with a non-equilibrium concentration of quasiparticles. When the nanowire is biased close to the critical current, this perturbation causes a transition from the superconducting to the resistive state, producing a voltage pulse in the external circuit.

While progress has been made in understanding the detection process, many crucial features of the process are still unknown. In this chapter, we investigate the detection process by means of a model system: an NbN nanodetector [39] (see Figure 3.1). This detector has a single cross section of wire as its active element, defined by a bow-tie shaped constriction. We investigate this system with sparsity-based detector tomography. The tomographic method does not require a model of the device, which makes it ideally suited as a tool for investigating the working principle of a detector of which the working mechanism is not fully understood yet.

It has long been known that at lower bias current, the detector operates in a regime where multiple photons are necessary to break the superconductivity [1, 66]. In a nanodetector, the geometry is such that many multiphoton processes play a strong role [39, 67]. This enables us to probe the response of the device to excitations at different energies simultaneously. The role of detector tomography is to extract the effects of the various multiphoton excitations.

In this chapter, we investigate the detection process by combining tomography and a nanodetector. With this combination, we can probe the system in a way that is independent of the incoupling efficiency of light into the detector. Moreover, because we tune the energy of the excitation via the number of photons at the same wavelength, we are insensitive to wavelength-dependent effects in the setup. This combination allows us to focus on the fundamentals of the detection process. We demonstrate that for intrinsic detection probabilities ranging from 0.3 to 10^{-4}, the detection probability depends only on a specific linear combination of bias current and excitation energy. Thus, we obtain a universal detection curve for our model system of an SSPD: for each bias current and excitation (photon) energy, the detection probability is given by a point on this single curve. This universal curve stretches from the regime where photodetection is almost deterministic (given that the photon is absorbed into the active area) to the regime where fluctuations in the wire are thought to play a role in assisting the detection process.

3.2 Experiment

All experiments in this work were performed on a nanodetector (see Figure 3.1). The nanodetector consists of 4 nm thin NbN wire on a GaAs substrate, shaped into a 150 nm wide bow-tie geometry. The device was fabricated via

a combination of DC magnetron sputtering [47], electron-beam litography, reactive ion etching and evaporation of the metal contacts [39]. In Chapter 2 and ref. [39] it was shown that such a detector has multiphoton regimes based on the bias current. The physical mechanism behind these multiphoton regimes is that at relatively low bias currents, multiple photons are required to supply a sufficient perturbation for the superconductivity to be broken.

The device was cooled in a two-stage pulse-tube / Joule-Thompson cryocooler to a temperature of approximately 1.2K. The nanodetector was illuminated using a lensed fiber mounted on cryogenic nanomanipulators. At this temperature, the overall system detection efficiency for single photons was 1.5×10^{-4} around our working point at $I_b = 20\,\mu$A ($I_c = 29\,\mu$A) . This low efficiency is attributable to the mismatch between the device active area and the size of the illumination spot. The device was operated in a voltage bias regime, using a low-noise voltage source (Yokogawa GS200) in series with a 10 Ω resistor. The detector was biased through the DC port of a bias tee, and the RF signal was amplified in a 45 dB amplifier chain.

The device was illuminated with a Fianium Supercontinuum laser, whose pulse duration was specified to be 7 ps. It is crucial for this experiment that the pulse duration is shorter than the lifetime of an excitation, which was measured to be several tens of picoseconds [40, 68, 69]. If the pulse duration is longer than that, it is possible to have a pulse which produces two excitations which are far enough apart in time that one has died out before the second is created; this will therefore not result in a multiphoton excitation.

We confirmed that our laser produces coherent states, measuring $g^{(2)}(\tau = 0) = 0.98 \pm 0.01$ in a separate experiment. Furthermore, we measured that the intensity fluctuations in the laser are below 2%. Hence, the laser is suitable for tomography [37]. The detector was illuminated with narrowband light at wavelengths of 1000 nm, 1300 nm and 1500 nm ($\Delta\lambda$= 10 nm). In our experiment, we vary the intensity and wavelength of the input light, at various bias currents. At each of these settings, we record the count rates in a 0.1 s time window and repeat the experiment 10 times per measurement setting. In the current regime investigated in the present experiment, the detector has negligible dark counts (< 1 / s).

3.3 Tomography of Multiphoton Excitations

In order to distinguish the effects of the various photon numbers in the laser pulses, we make use of a sparsity-based tomographic protocol. We give here a brief summary of this protocol (for a full description, see Chapter 2, where we introduced this technique). We illuminate the detector with a range of coherent states, and record the detection probability R_{click}. We make use of two properties of coherent states: first, that a coherent state under attenuation remains coherent, second that the decomposition of the coherent

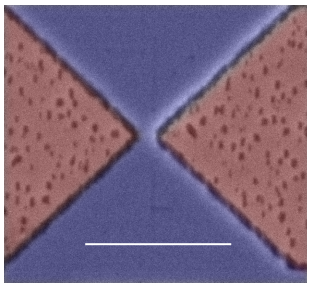

Figure 3.1: False-color SEM image of the detector. The active part of the detector is the narrow bridge in the centre of the image. The blue parts represent the thin layer of NbN, the red parts are the GaAs substrate. The scale bar has a length of 1 μm.

state in the Fock basis is completely determined by the mean photon number, which can be determined by measuring the intensity[2].

Each illumination intensity probes the detector with a different linear combination of photon number states, introducing different combinations of multiphoton excitations. In particular, we model the detection probability R_{click} by:

$$R_{click} = 1 - e^{-\eta N} \sum_{n=0}^{\infty} (1 - p_n) \frac{(\eta N)^n}{n!}, \tag{3.1}$$

where η is the incoupling efficiency (linear loss) and N is the mean photon number of the incident coherent state. The linear efficiency appears separately, since our protocol enables us to distinguish linear processes - such as incoupling to the NbN film - from nonlinear processes [67]. The p_n are the quantities of interest in further analysis: they describe the probability of a detection event, given the absorption of n photons in the active area of the detector.

Figure 3.2 illustrates this protocol as applied to a single experimental run for a given bias current. We vary the incident power, observe the detection probability, and apply the tomographic protocol to find the contributions from the various multiphoton excitations. The black squares indicate the measured count probability, approaching 1 as the detector saturates. The red, green and blue lines indicate the contribution from one photon, two photons and higher photon numbers, respectively. Only a limited number of multiphoton excitations are resolvable, and this number depends on bias current. The rest is lumped into a remainder term containing the limit of high photon numbers and is not used in further analysis. The fact that at various powers different multiphoton processes are dominant enables us to recover them all from a single experiment. Furthermore, since the linear

[2]Since we have a phase-insenstive detector, the phase of the coherent state amplitude is irrelevant, and we set it to zero throughout this chapter for simplicity.

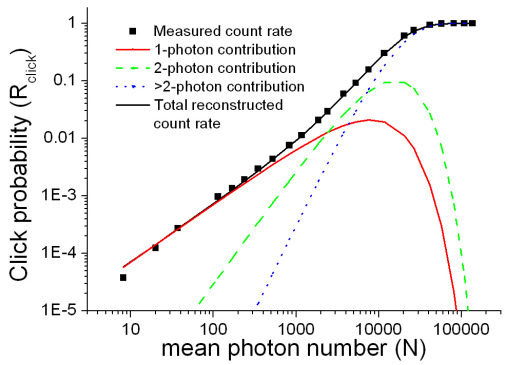

Figure 3.2: Illustration of the tomographic protocol. The black squares indicate the measured count rate as a function of input power, at $\lambda = 1500$ nm and $I_b = 17\,\mu$A. The red (solid) and green (dashed) lines show the contribution to the count rate of single photons and photon pairs, respectively. The blue (dotted) line shows the contribution of higher numbers of photons. The black line shows the sum of all the photon contributions, indicating that our tomographic reconstruction succesfully reproduces the observed count rates. From this fit, we reconstruct the set of detection probabilities p_n and the linear efficiency η, which together fully describe the behaviour of the detector.

efficiency η only rescales the effective incident photon number, but does not alter its shape (corresponding to a simple shift in Figure 3.2), we are also able to distinguish finite incoupling effects from effects due to multiphoton excitations.

3.4 Results

Figure 3.3 shows the reconstructed detection probabilities p_n, as a function of bias current and three different wavelengths. For each wavelength and current, we independently perform the tomographic procedure outlined in Section 3.3 and obtain a full set of parameters p_n. We observe that as the current is lowered, the detector makes a transition from being a one-photon threshold detector to a two-photon threshold detector, and so on. Furthermore, we observe that the response curves at different photon numbers and wavelengths have the same shape. We note that as the excitation energy becomes higher and the photon number larger, the points on our curves become more scattered, indicating that the tomography procedure becomes less accurate.

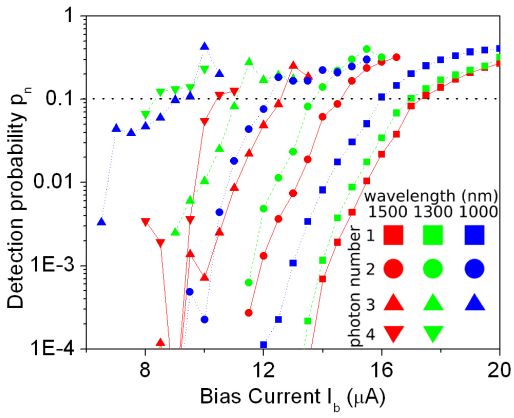

Figure 3.3: Current dependence of the nonlinear parameters p_n , as a function of wavelength and photon number. The probability p_n of a detection event at a given wavelength and photon number is plotted as a function of the current. The plots are color-coded by wavelength. The shape of the symbols indicates the photon number (see legend). The connecting lines are a guide to the eye. The dotted line indicates the threshold level (p = 0.1) used to obtain Figure 3.4.

Figure 3.4 shows the bias current required to reach a detection probability of 10%, as a function of total excitation energy. In order to obtain this figure, we took a surface of constant $p_n(E, I_b) = 0.1$ in Figure 3.3 (indicated by a dotted line), and plotted the bias current at which the detector has 10% probability of responding to an energy E, where $E = nh\nu$ is the total energy of the n photons absorbed by the detector. This figure demonstrates that there is a scaling law between bias current and overall excitation energy. We determine the scaling constant γ to be γ = -2.9 $\pm$ 0.1 μA/eV (= -1.8×10^{13} Wb^{-1} in SI units) for our detector. Furthermore, this figure shows that the detection probability is independent of the way in which the excitation is composed of different photons: only the overall energy determines the detection probability. We note that we have used only a small fraction of the data present in Figure 3.3 to obtain the data presented in Figure 3.4.

We compare three models from literature to our data. We find that over the range of the experiment, all three models are consistent with our data. The three models are a hotspot-based model, a hotspot-based model in which diffusion plays a large role and a fluctiation-assisted model. These models distinguish themselves not only by different detection mechanisms, but also by different scaling between bias current and energy at constant detection efficiency.

Figure 3.5 presents the main result of this chapter: a universal detection

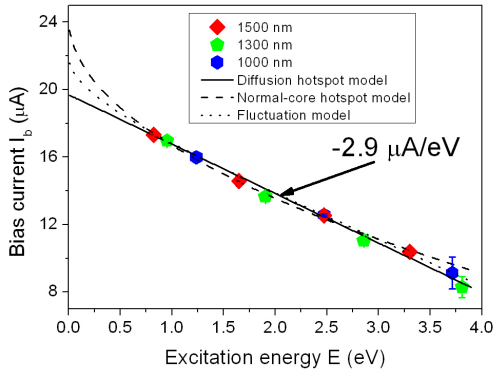

Figure 3.4: Scaling law for the nanodectector. From the data in Figure 3.3, we find all points that have $p_n(E, I_b) = 0.1$ (indicated by the dotted line in that figure), where E is the overall excitation energy. In this graph, we plot the values of I_b and E that satisfy this condition. This graph shows that bias current and overall excitation energy have an approximately linear dependence. The fact that points at various photon numbers all fall on the same line demonstrates that the nanodetector is only sensitive to the overall energy of the excitation. The three lines show the fits of the three microscopic models to the data. Apart from the two rightmost points, the errors on these data points are ~ 100 nA.

curve for a single line-segment of an NbN SSPD. In Figure 3.5, we apply the scaling law, which was derived from the points around $p = 0.1$ to the entire data set. We find that all the curves of detection probability as a function of rescaled bias current superimpose over more than 3 orders of magnitude in the detection probability. This shows that the photoresponse of our detector depends only on this specific combination $I_b + \gamma E$ of bias current and excitation energy. We stress that this universal curve can only be obtained through detector tomography, which allows separation of the effects of multiphoton excitation and finite linear efficiency.

The data presented in Figure 3.5 shows that the scaling behaviour which we obtained at $p_i = 0.1$ in Figure 3.4 is universal for all values of p. Since we have used only the points in Figure 3.3 which lie around to obtain the result in Figure 3.4, we do not a priori expect the curves to superimpose when we apply the scaling law to the entire dataset. In such a procedure, only the points which are used to obtain the scaling factor are guaranteed to superimpose. Since the curve is universal over more than 4 orders of magnitude in the detection probability, we have demonstrated that our results are independent of the arbitrary choice of the 10% criterion. The criterion only matters for the accuracy with which the curves can be superimposed:

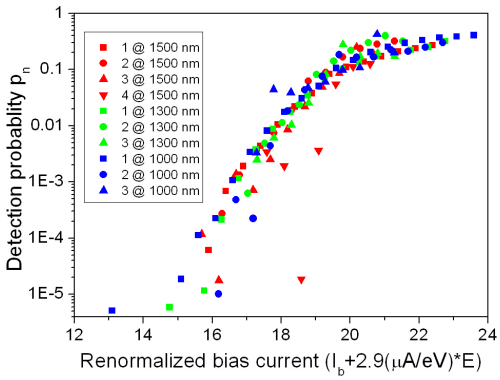

Figure 3.5: Universal response curve for the nanodetector. To obtain these curves, we rescale the curves reported in Figure 3.3 by the scaling law demonstrated in Figure 3.4.

we find from theoretical simulations that the tomographic reconstruction is most accurate between $p_n = 0.1$ and $p_n = 10^{-4}$. This justifies the choice of our criterion.

3.5 Discussion

In this section, we first compare our experimental method with that of previous studies on SSPDs. Then, we discuss our experimental findings on the universal curve, quasiparticle conversion efficiency. Lastly, we discuss the phenomenon of dark counts in our detector.

3.5.1 Comparison with Previous Work

Previous investigations of the SSPDs detection mechanism were of a semiclassical nature, where only the efficiency and dark count rate were measured. By observing the exponent of the power-law dependence of count rate on input power, one can also infer the photon number detection regime semiclassically. However, such a characterization is limited to the observation that the detector is operating in a particular detection regime; a measurement of p_i (i.e. how strongly the detector is in a particular regime) requires detector tomography. Since the width of each multiphoton regime is ~ 2 μA for our experiment, the accuracy of the semiclassical method is rather limited. In order to characterize multiphoton processes beyond that resolution, detector tomography is an absolute requirement.

Most previous work focussed on meander detectors, which is the geometry that is normally used in practical applications of SSPDs. In a meander,

two photons that are absorbed in different places along the wire do not constitute a two-photon event, yet they may still produce one-photon events individually. By using a nanodetector, we sidestep any question of how the photons distribute themselves along the length of the wire, which was a major issue in measuring multiphoton effects in meander-type SSPDs [43, 44].

Our present work probes the detection mechanism at various energies simultaneously. We are insensitive to incoupling losses, since they affect the various multiphoton processes equally. Furthermore, since we can perform excitations at different energies with the same wavelength, we are insensitive to any wavelength-dependent effects in the experiment, including wavelength-dependent absorption in the NbN layer.

3.5.2 Universal Curve

The universal curve which we demonstrate in Figure 3.5 is not predicted by any of the current SSPD photodetection models. Typically, such models focus on calculating a single threshold bias current I_{th}, above which the energy of a photon is large enough to deterministically break the superconductivity. Above that current, the efficiency of the detector should be constant. We have shown in the present work that scaling behaviour extends not just to a single threshold current, but to all combinations of currents and excitations in the present experiment. Scaling behaviour applies whether one is in the regime of high effiency or not. This points to the fact that a single theory should describe detection events in SSPDs, both in the high- and low-efficiency regimes.

3.5.3 Quasiparticle Conversion Efficiency

The fact that only the overall energy of the excitation determines the response of the photodetector can be interpreted in terms of the cascade process that is generated by the initial excitation. This process, which is thought to involve both electrons and phonons in the film, and in which the mutual exchange of energy between the electron and phonon subsystem plays a key role, is still poorly understood. In the present work, we probe this cascade process with different initial excitations, and show that it is only the overall energy which determines the total number of quasiparticles which are produced at the superconducting band-edge. The fact that four excitations of a quarter of the energy produce the same number of quasiparticles as a single excitation with the full energy is evidence that the conversion efficiency by which the energy of the first quasiparticles is distributed over many others is independent of the initial energy.

3.5.4 Dark Counts

We now turn to the phenomenon of dark counts. The most straightforward model is the following: one simply considers a dark count as an excitation with $E = 0$. Extrapolating the linear scaling law from Figure 3.4 to $E = 0$ yields a current of 19 μA. However, at this current we do not observe a dark count probability of 10% as one would expect from the simple model; we only observe appreciable dark counts around the critical current of 29 μA. The same discrepancy applies to the other two models. We can therefore say that the picture of a dark count as a zero-energy photodetection event is not supported by our data for any current detection model of SSPDs. The anomalous behaviour of dark counts is a reminder of the danger of assuming a detection model, further demonstrating the relevance of our tomographic method. In particular in this case, the tomographic method gives the first hints of substantial differences in detection mechanism between dark counts and photon counts. We note that the nature of dark counts is still open to debate [24, 70, 71].

3.5.5 Outlook

The present work opens up the possibility of testing the various models of photodetection. This could be done by performing the present experiment in the mid-infrared. For this energy range the predictions of the various models differ significantly (see Figure 3.4). For example, at an excitation wavelength of 5 μm, corresponding to 0.25 eV, the difference between the predictions of the various models is easily measurable; it is of the order of 1 μA.

Multiphoton excitation has the practical advantage that the bandwidth of energy excitations which is offered can be extended by a factor equal to the number of photons in the highest excitation (in our case, 4). This has applications in the situation where light of a particular wavelength is difficult to couple onto a cryogenic sample. In particular, the present work opens up the possibility of studying NbN detector behaviour in an energy range that corresponds to the near and medium UV range, using visible and NIR optics.

In a previous publication [40], we have introduced the notion of the nonlinear response function (NRF) $\eta(I_b, C)$, which measures the instantaneous detection probability, given that a bias current of I_b is present, and that there are C quasiparticles in the detector. The overall detection probability is then given by $\mathrm{R} = \int_t \eta(t) I(t) dt$, where I is the instantaneous intensity. This function can be probed by various means such as a pump-probe experiment. The description in terms of a NRF is well-matched to a tomographic experiment, as both are model-independent descriptions.

The holy grail of tomographic research on SSPDs would be to find the instantaneous detection probability as a function of the number of quasiparticles present at that instant. In the present experiment, we have achieved

a step towards this goal: we have demonstrated the NRF to be of the form $\eta(I_b + \gamma E)$ over the energy range of the experiment, for short-pulse excitations.

3.6 Conclusion

In conclusion, we have studied the physics of photodetection in a superconducting single-photon detector. We have shown that the probability of detection is based on the overall energy of the excitation. Furthermore, we have demonstrated a scaling law between overall excitation energy and bias current. From this, we find a universal response curve that depends only on a given combination of bias current and excitation energy. Thereby, we have shown that the known behaviour of the detector extends into the multiphoton range. These results demonstrate that the tomographic method is a useful tool for investigating the fundamental physics of detection events in NbN SSPDs.

3.i Appendix: Comparison of Experimental Data with Detection Models[3]

We compare our experimental results to the various detection models of superconducting single-photon detectors. We consider three models: the normal-core model, the diffusion-based model and an early version of a vortex-based model, namely the VAP model of Semenov *et al*[4]. We parameterize these models as: $E = w^2/C^2(1 - I_b/I_c)^2$ for the normal-core hotspot model, $I = I_0 - \gamma E$ for the diffusion model and $A = (\Delta - \alpha\sqrt{E})(I_0 - \beta I_b)$ [72] for the VAP model, to maintain consistency with the literature.

We apply these three detection models to the results in Figure 3.4, and compare the results with the values from the literature. For the normal-core hotspot model, we find $C = 47 \pm 1$ eV$^{-1/2}$/ nm, which should be compared to the values of $C = 11-20$ eV$^{-1/2}$/ nm found in other experiments [56]. For the diffusion hotspot model, we apply the expression from Ref. [8], to find a theoretical value of γ = -2.5 μA/eV for our sample and γ = -3.5 μA/eV for the samples in that reference, which should be compared with the value of γ = -2.9 $\pm$ 0.1 μA/eV obtained experimentally. For the fluctuation model, we find $\alpha = 2.8 \times 10^{-4} \pm 0.05 \times 10^{-4}\sqrt{\text{eV}}$, which should be compared to a literature value of $\alpha = 6 \times 10^{-4}\sqrt{\text{eV}}$, for the experiment reported in Ref. [23]. We note, however, that comparisons between different detectors are problematic. In particular, the conversion efficiency of the initial excitation to quasiparticles at the gap edge is a free parameter which varies from detector to detector [8].

The error analysis on the quantities given in the previous paragraph was based on the 50 nA accuracy of the current readout of our experiment, combined with error propagation on the interpolation formula used to obtain the intersection with the line $p_i = 0.1$. For low i, the former error dominates. At higher i, we are limited by the quality of our tomographic reconstruction. We calculate $\chi^{(2)}$ per degree of freedom to be 2.2, 2.9, and 2.1 for the normal-core hotspot, diffusion hotspot and VAP models, respectively. These numbers do not enable us to conclusively rule out any of the models.

[3] This material is based on the appendix to J.J. Renema *et al.*, Phys. Rev. B **87** (17), 174526 (2013).

[4] We retain the comparison with the VAP model for historical consistency with the article on which this chapter is based. Since we will see that this dataset is of insufficient dynamic range to rule out any of the models, comparison with more advanced vortex models will not provide additional information and is postponed to Chapter 4.